INDONESIAN JOURNAL OF GEOGRAPHY

RESEARCH ARTICLE

Investigation of a Relation between Radiogenic Heat Production Rate (RHPR) and Land Surface Heat Temperature (LST) from Thermal Bands of ASTER and Landsat-8 (TIR-Data): Case Study of West Ras Gharib area North Eastern Desert, Egypt

Samah S. Abdeen[1], Samy H. AbdElnaby[2], Moataz E. El-Manawy[1], Reda A. Al-Arafy[1], and Karam S. Farag[2]
[1]Nuclear Materials Authority, Cairo, Egypt, [2]Faculty of Science, Ain Shams University, Egypt

Abstract. In this paper, an attempt was tried to study the relation between the land surface heat temperature (LST), extracted, from the thermal emission infrared data (ASTER-TIR) and (Landsat-8-TIR) imagery and radiogenic heat production rate (RHPR) that calculated from airborne gamma-ray spectrometric data applied on west Ras Gharib area at Northeastern Desert of Egypt. The area is geologically covered mainly by Precambrian basement rocks, which are unconformably overlain by Phanerozoic sedimentary succession. The method used for extraction land surface heat temperature for both ASTER-TIR and Landsat-8-TIR images is the reference channel emissivity technique and founded as the best method comparing to others. The study results showed a relative higher RHPR threshold value reached 4.8 μW/m3. On the other hand, ASTER-TIR Land Surface Temperature (AST-LST) ranges between 27.64oC to 47.2oC and, the Landsat 8-TIR Land Surface Temperature (LS8-LST) ranges between 30.64oC to 50.68oC. Comparing all results, there were a weak relationship or to some extent parallel relation between RHPR and satellite LST; as when the value of the Y-axis is constant, there are multiple values on X-axis, so it is not possible to deduce the value of one variable in terms of the other. The poor relation is regarded to the very weak RHPR which is not enough to affect the surface heat temperature, emission that could be detected by both thermal sensors of ASTER and Landsat-8 satellite TIR data. Other factors such as: topography, wind, shading and scattering, rock moisture and density, can strongly affect the surface temperature. In conclusion, the output results could be improved in areas of very high radioelement concentrations especially 235U, and through the use of the enhanced spatial resolution of future satellite TIR imaging instruments.

1. Introduction

The cooling of the Earth and the heat produced by radioactivity releasing heat that appears to be primarily responsible for the heat flow detected at the Earth's surface and the temperature distribution within it. The amount of radio-elements existing in the rocks releases sufficient heat to account for a great portion (typically, 60 % for continental crust) of the entire heat flow detected on the Earth's surface (Gupta and Roy, 2007). Table 1 shows the relevant details of half-life and heat production by the most commonplace radioactive elements in rocks (Ladislaus Rybach, 1976).

The radiogenic decay of the unstable isotopes of Uranium (U238, U235), Thorium (Th232) and Potassium (K40) delivers the largest internal source of heat; these radionuclides are enriched in the Earth's crust and mantle (McDonough and Sun, 1995; BEA, 1996; Jaupart et al., 2015; Stacey and Davis, 2008; El-Said, 2014). Throughout the radioactive decay process, emission of α, β and γ particles convert into radiogenic heat. The amount of radiogenic heat produced per unit time (i.e., the rate of radiogenic heat production) created from rocks is independent of

occurrence forms, temperature and pressure of the rocks, but only determined by the concentration of the radioactive nuclides in the rocks (Zhang et al., 2007). Most of the potassium is located in K- micas and feldspar, whereas uranium and thorium are basically found in the accessory minerals such as; monazite, allanite, sphene, zircon, and apatite (BEA, 1996). These minerals are wide speared in granitoids rocks, which, therefore, account for the extent of heat production in the continental crust (El-Said, 2014).

Radiogenic heat production rate (RHPR) is a physical property that outlines the extent of heat liberated in a unit volume in a unit time of rock by the decay of unstable radiogenic isotopes (Clauser, 2011). RHPR is also used for the description of temperature differences with depth and interpretation of current heat variation (Salem et al., 2004). The abundance and spreading of these heat sources are of dominant importance in studies on the terrestrial heat fluidity of the lithosphere (Pasquale et al., 1999, 2001). Radiogenic heat production detection was reported in several research papers by many authors by using the

measured spectrometric data survey and extracts the heat from it (e.g., Cermak et al., 1982; Van-Schmus, 1984; Stacey and Davis, 2008; Jaupart et al., 2015; Clauser, 2011; Adagunodo et al., 2019; Farag et al., 2020; Pleitavino et al., 2021).

Remote sensing can utilize in geothermal studies and mineral explorations by identifying surface thermal anomalies using the thermal infrared (TIR) bands of satellite imagery. Thermal infrared remote sensing delivers a distinctive tool for representing the surface expressions of geothermal activity. In thermal remote sensing, radiations emitted by ground objects are measured for temperature estimation. These measurements give the radiant temperature of a body which depends on two factors (kinetic temperature (Land surface temperature) and emissivity) (Prakash, 2000).

Land surface heat temperature (LST) terms as how warm the Earth's surface would sense to the touch in a particular location. From satellite's perspective, the "surface" is whatever it realizes when it gazes through the atmosphere to the ground. This surface could be the roof of a construction, the grass, snow, or the leaves in the awning of a forest. Thus, LST is not similar to the temperature of air which is involved in the daily weather report (Mather and Koch, 2011).

Investigation a relationship between RHPR and LST on west Ras Gharib area is the main objective of this paper that may aid in developing a uranium exploration program using satellite TIR-remote sensing imagery. This will be used as a guide for further recommendations and follow-up radioactive elements exploration work.

West Ras Gharib area is located in the Northern part of the Eastern Desert; this sector is notable for its variety of economic mineral occurrences. The study area lies between latitudes 28° 00` to 28° 41` N and longitudes 32° 20` to 33° 00` E and occupies an area of approximately 2322 Km2 (Bühler et al., 2014) (Fig.1).

The investigated area is a part of the Arabian–Nubian Shield that was discussed by many researchers. Topographically, the study area is characterized by relatively high relief, especially the younger granite bodies at which there are a number of summits exceeding 1000 m above the sea level (Conoco, 1987) (Fig.2). Geologically, the geologic outcrops of the area show a different range of stratigraphic rock units from Proterozoic to Phanerozoic. Phanerozoic rocks composed of, Quaternary sediments, Sudr Formation, Galala Formation, Wadi Qena Formation, Samr El Qaa Formation and Araba Formation and are occupied mainly
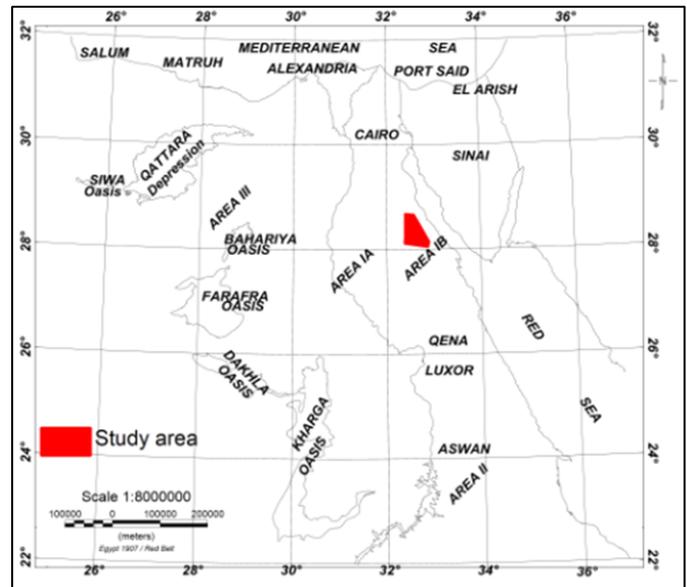

Figure 1. Location of West Ras Gharib area, North Eastern Desert, Egypt
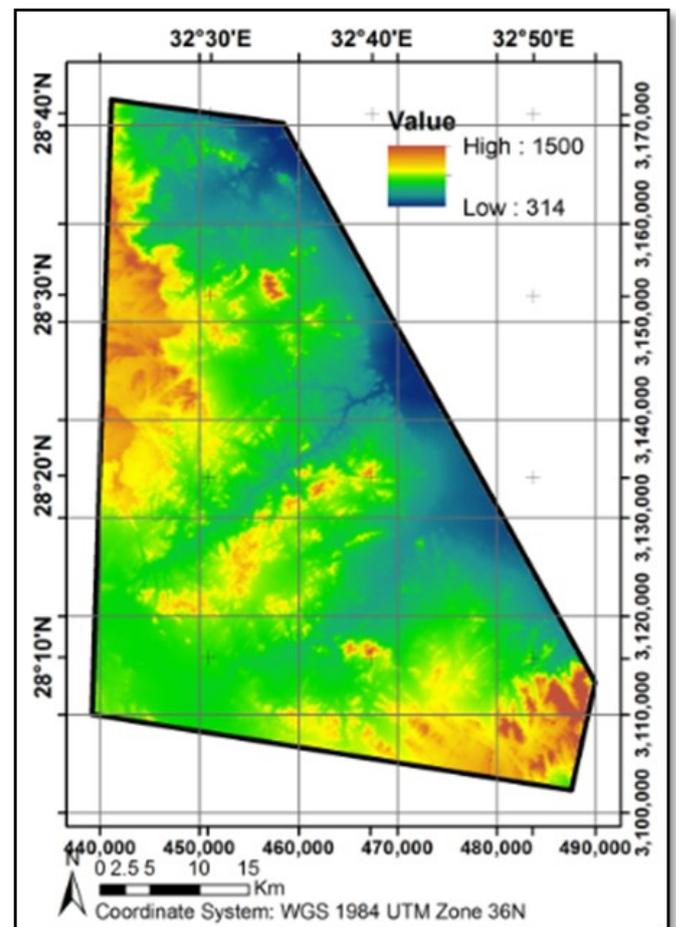

Figure 2 Topographic elevation map (TEM) according to SRTM World Wide Elevation Data (1 arc-second Resolution) of West Ras Gharib area, North Eastern Desert, Egypt (Farr and Kobrick, 2000; Rosen et al, 2000; Kobrick, 2006; Farr et al., 2007)

the western part of the study area (Said, 1990; Ammar et al., 2007). (Precambrian Basement Rocks) which composed of, Dokhan Formation, Younger Granite, Older Granite, Metavolcanics and Metagabrro-Metadiorite. They are occupied mainly in the central and eastern part of the study area (Said, 1990; Ammar et al., 2007) (Fig.3)

Table 1. Major Radioactive Isotopes Found in Rocks, Their Half-Lives and Heat Production (Rybach 1976)

Isotopes	Half-life (year)	Heat production (J $Kg^{-1}year^{-1}$)
^{238}U	$4.50*10^9$	$2.97*10^3$
^{235}U	$0.71*10^9$	$18.01*10^3$
^{232}Th	$13.9*10^9$	$0.83*10^3$
^{40}K	$1.30*10^9$	$0.92*10^3$

2. Methods
Data Acquisition

Aerospectrometric Data. Was surveyed by Aero-Service 1984 with specification; the flight (traverse) lines were oriented in a NE-SW direction with an azimuth of 45°and 225° and spacing 1.5 km approximately. The tie lines were oriented in a NW-SE direction with an azimuth of 135°and 315°and spacing of 10 km approximately.

Advanced Space Borne. Thermal Emission and Reflection Radiometer (ASTER) Sensor is a cooperative effort between the Japanese Ministry of Economic Trade and Industry (METI) and National Aeronautics and Space Administration (NASA). It is a high spatial, spectral, and radiometric resolution multispectral remote sensing instrument launched on NASA's Earth Observing System (EOS AM-1) near polar-orbiting, sun-synchronous orbit at 705 km altitude spacecraft, Terra in December 1999 (Pour and Hashim, 2012). ASTER recurrent cycle (temporal resolution) is 16 days, with additional 4-day repeat coverage due to its off-nadir pointing capabilities (Wulder et al., 2019). The ASTER Level_1B data which geometrically and radiometrically calibrated was produced at the USGS Earth Resources Observation and Science (EROS) data center.

Figure 3. Geological map of West Ras Gharib area, North Eastern Desert, Egypt, (Modified after Conoco, 1987)

The area of study is covered by one scene (Fig.4). Table 2 shows the characteristics of the selected scene. ASTER represented by fourteen spectral bands in the visible and near-infrared (VNIR), the short-wave-infrared (SWIR), and in the thermal infrared (TIR) regions (Erdi-Krausz et al., 2003). (Table 3). TIR sensor with 5 spectral bands is useful for defining surface temperature and silica contents. Each ASTER scene covers an area of about 60×60 km. A numerous studies have used ASTER data to distinguish surface geothermal anomalies by minimizing the temperature variations caused by diurnal solar heating effects (Coolbaugh et al., 2007; Eneva et al., 2007; Eneva and Coolbaugh, 2009).

Landsat 8 Sensor

Landsat 8 Sensor is the eightieth satellite of the Landsat program but the seventh in reaching orbit successfully. Landsat 8 was launched on 4th February 2013 from Vandenberg Air Force Base in California. It is an American Earth observation satellite. The study area is covered by one scene was obtained from the US Geological Survey Earth Resources Observation and Science Center and downloaded in TIFF format (Fig.5). Landsat-8 image represented by eleven bands; five of them in the visible and Near-Infrared (VNIR) with spatial resolution 30 m, two in the SWIR domain with spatial resolution 30 m and one in Pan Region and one panchromatic channel (band eight) with spatial resolution 15 m. TIR bands are two in the Thermal Infrared (TIR) domain with spatial resolution 100 m (Table 4). Table 5 shows the characteristics of the selected scene.
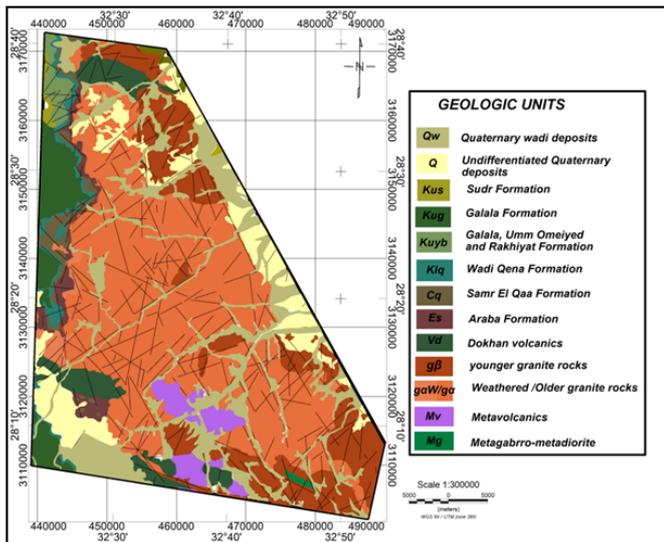
Table 2. The ASTER Scene Characteristics of The Studied Area

Level	AST_L1B
Scene No.	08434020120
Date of acquisition	2 July 2001
Time of acquisition	8:29:22Z
Cloud cover	0%
Scene size	60*60 Km^2

Table 3. ASTER Bands Characteristics:

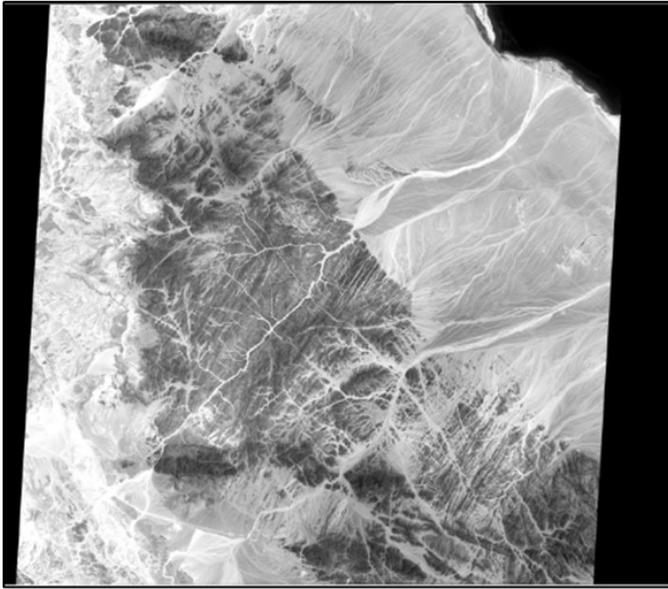| Characteristics		VNIR		SWIR		TIR
	Band (1)	0.52-0.60 Nadir looking	Band	1.6-1.7	Band	8.125-8.475
	Band (2)	0.63-0.69 Nadir looking	Band	2.145-2.185	Band	8.475-8.825
	Band (3N)	0.76-0.86 Nadir looking	Band (6)	2.185-2.225	Band (12)	8.925-9.275
Spectral range (μm)	Band (3NB)	0.76-0.86 Backward look-	Band (7)	2.235-2.285	Band (13)	10.25-10.95
			Band	2.295-2.365	Band	10.95-11.65
			Band	2.36-2.43		
Ground resolution		15m		30 m		90 m
Swath width		60Km		60 Km		60 Km
Signal quantization		8bits		8 bits		12 bits

Figure 4. The ASTER Scene of West Ras Gharib Area, North Eastern Desert, Egypt
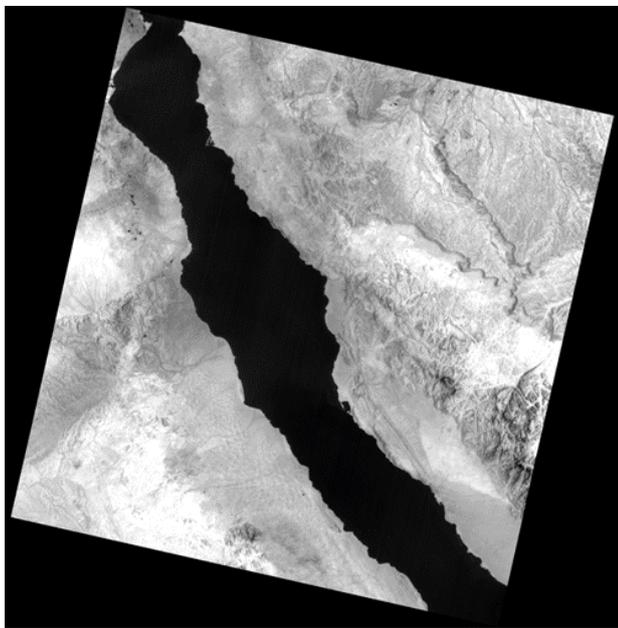

Figure 5 .The Landsat 8 scene of West Ras Gharib area, North Eastern Desert, Egypt

Presentation of Airborne Gamma-Ray Spectrometric Survey Data

Geophysical measurements of surface or subsurface materials are made either at isolated points or along lines as a more or less continuous one-dimensional record (Drury and Walker, 1987). Thus, contour maps cannot fully define all the information available from geophysical data so, they were converted to raster images through interpolation and gridding into gray scale of 8 bits (256 levels) to be suitable for further image processing techniques. The results of spectrometric data distribution over the area of Ras Gharib .

Total Count (TC) µR/h Map

The TC map (Fig. 7a) shows three radiometric levels: high, inter-mediate and low. The high level indicates values exceeding 8.5 µR/h (from red to magenta) and located mainly at the southeastern corner (G. Ras Gharib), at northeastern part (G. Umm Tinassib) and some dispersed spots at central parts of the study area trending NE-SW. The intermediate level ranges from 4.9 to 8.5 µR/h (from green to yellow) located at the central part of the study area trending NE-SW and the low radiometric concentration level is less than 4.9 µR/h (from blue to cyan) and recorded at the western parts of the study area.

Equivalent Uranium (eU) ppm Map

The eU map (Fig. 7b) can be classified into three levels: the first level having eU up to 3.1 ppm (from red to magenta) and recorded as dispersed spots mainly at the Northeastern (at G. Umm Tinassib) and at Southeastern parts (at G. Ras Gharib) and central parts trending NW-SE of the study area. The intermediate level ranging from 1.8 to 3.1 ppm (from green to orange) are classified as intermediate values of the second level, which are located at most of study area

Table 4. The Landsat 8 Scene Characteristics of The Studied Area

Scene	LC81750402019177LGN00
path/ row	175/ 40
Date of acquisition	26 June 2019
Time of acquisition	08:17:57.763965Z
Scene size	185 * 180 Km^2

Table 5. LANDSAT-8 Bands Characteristics

Sensor	Subsystem	Band number	Spectral range (µm)	Ground resolution (m)	Swath width (Km)
Landsat-8	VNIR	1	0.433-0.453	30	185
		2	0.450-0.515		
		3	0.525-0.600		
		4	0.630-0.680		
	SWIR	5	0.845-0.885		
		6	1.560-1.660		
		7	2.100-2.300		
	Pan	8	0.500-0.680	15	
		9	1.360-1.390		
	TIR	10	10.30-11.30	100	
		11	11.50-12.50		

trending NE-SW. The low level (less than 1.8 ppm) (From deep blue to cyan) is recorded at the Western part of the study area.

Equivalent Thorium (eTh) ppm Map

The eTh map (Fig. 7c) can be categorized into three levels: the first level increases up to 9 ppm (from red to magenta) and recorded mainly at the northeastern corner (G. Umm Tinassib) and southeastern corner (G. Ras Gharib). The second level ranges from 5.4 to 9 ppm (from green to orange) and locates mainly at the central parts and at the central North part of the study area while the low level has eTh values less than 5.4 ppm (from deep blue to cyan). It is noticed that these low concentrations are recorded at the Western part of the study area.

Potassium (K%) Map

The K percent map (Fig. 7d) indicates that Cretaceous period formations: Galala, (Galala, Umm Omeiyed Hawashiya and Rakhiyat), Wadi Qena, Carboniferous formations: Samr El-Qaa, and Cambrian period formation: (Araba Formation and Quaternary wadi deposits) are representing the low level (less than 1.8 %); while the values ranging from 1.8 to 2.4 % (from green to orange) are classified as intermediate values of the second level, which are located at most of study area trending NE-SW. The third level is relatively a high concentration zone having K% up to 2.4 % (from red to magenta) and recorded as dispersed

spots mainly at the Northeastern part (at G. Umm Tinassib) and at Southeastern and central parts trending NW-SE of the study area.

Ternary (Composite) Images

A ternary image merging the three radioelements (K%, eTh ppm and eU ppm) images as red, green and blue (RGB) to give a significant radioelement ternary composite maps. Generally, ternary plots of the radioelements usually give a superior image of the geology (Salem et al., 2004). This can be seen in the good correlation between the ternary image (Fig. 8) and the mapped geology (Fig. 3). It was noticed that, the higher light zones are clearly correlated with granitic rocks which are normally characterized by their strong radiospectrometric responses and elemental differences; it's and recorded at the eastern part of the study area. Meanwhile, it shows black areas of weak radioelement contents as indicative to the low radioactive rocks as Cretaceous period formations and recorded at the Western part of the study area. The central part of the study area possesses high K concentration (red color) which geologically represented by older granitic rocks.

Ternary (Composite) Images

A ternary image merging the three radioelements (K%, eTh ppm and eU ppm) images as red, green and blue (RGB) to give a significant radioelement ternary composite maps. Generally, ternary plots of the radioelements usually give a
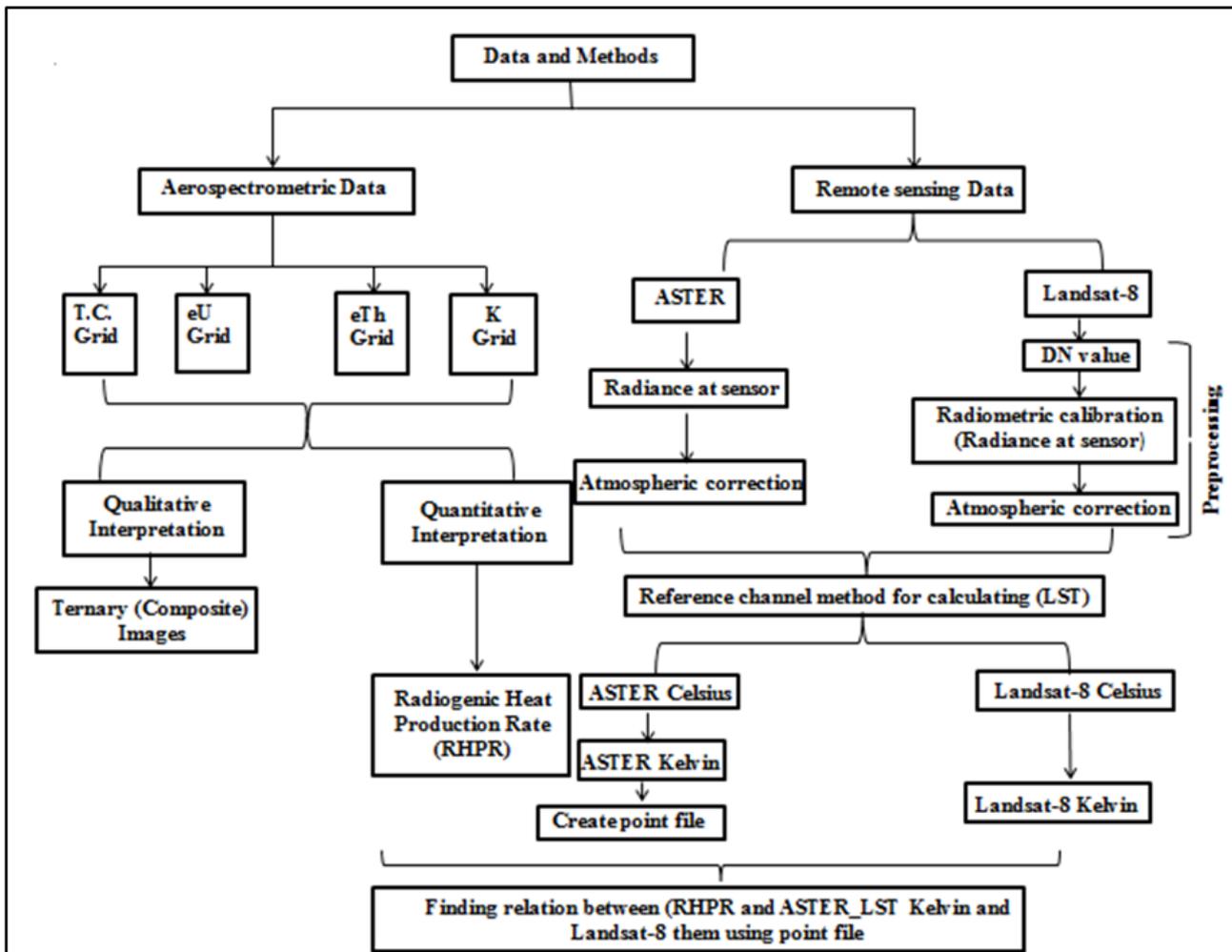

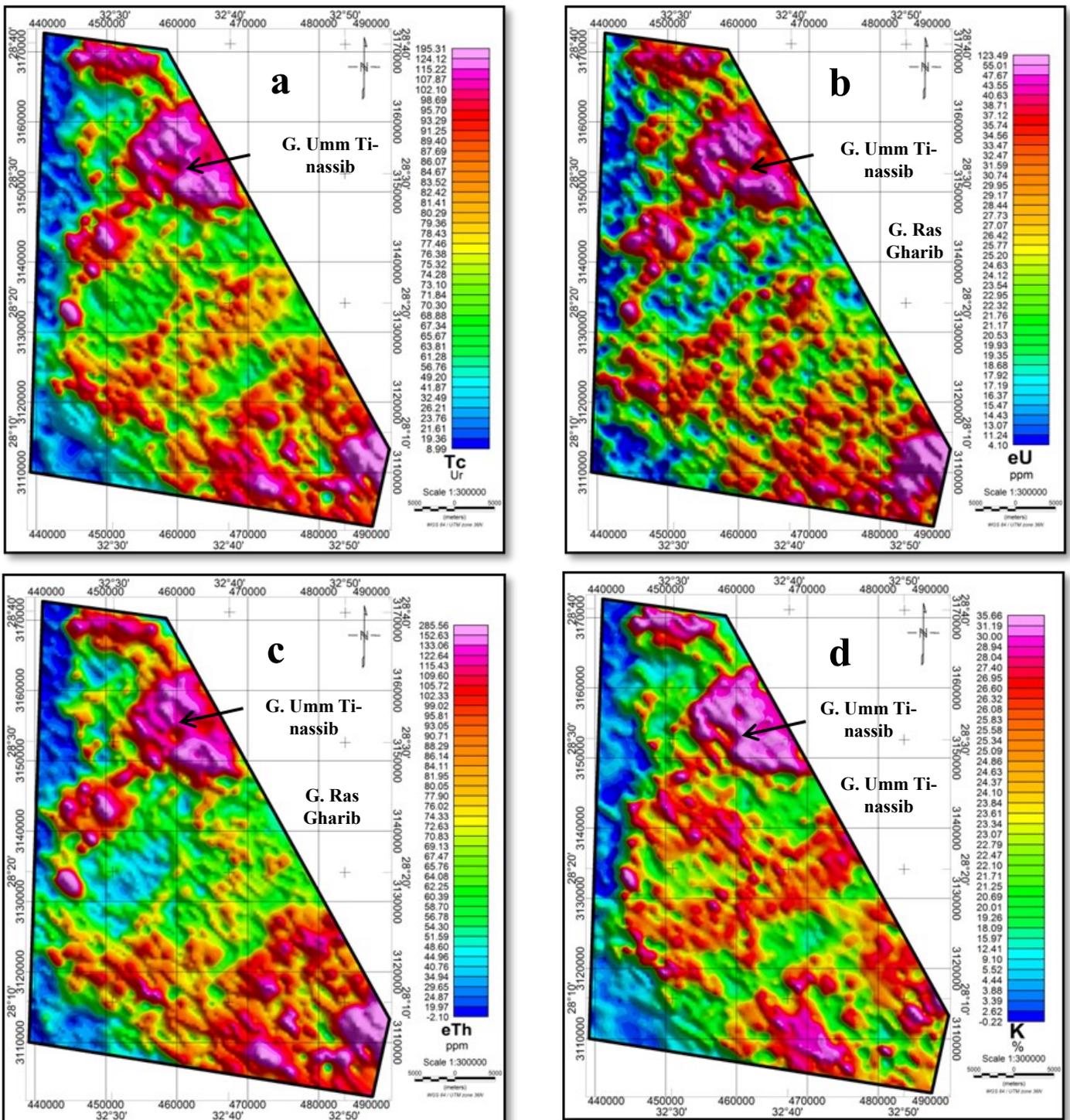Figure 6. Schematic diagram of the methodology used in the present study.

Figure 7. Filled color map of a) The total count radiometric data, b) The equivalent Uranium data, c) The equivalent Thorium data, and d) The Potassium data of West Ras Gharib area, North Eastern Desert, Egypt. (Data value * 10).

superior image of the geology (Salem et al., 2004). This can be seen in the good correlation between the ternary image (Fig. 8) and the mapped geology (Fig. 3). It was noticed that, the higher light zones are clearly correlated with granitic rocks which are normally characterized by their strong radiospectrometric responses and elemental differences; it's and recorded at the eastern part of the study area. Meanwhile, it shows black areas of weak radioelement contents as indicative to the low radioactive rocks as Cretaceous period formations and recorded at the Western part of the study area. The central part of the study area possesses high K concentration (red color) which geologically represented by older granitic rocks.

3. Result and Discussion
Calculating Radiogenic Heat Production Rate (RHPR)

Estimates of K, U and Th concentrations from gamma ray spectrometry can be used to approximation the radiogenic heat generated by rocks. Disintegration of the natural radionuclides in the earth is accompanied by the release of thermal energy (International Atomic Energy Agency (Erdi-Krausz et al., 2003). Radio-genic heat production of a rock is the total heat produced by the radioactive isotopes of U, Th and K. It is defined as the quantity of heat produced by radioactivity in unit volume of the rock per unit time and is expressed in microwatts per cubic meter. The kinetic energy of the emitted particles and the gamma-radiation associated
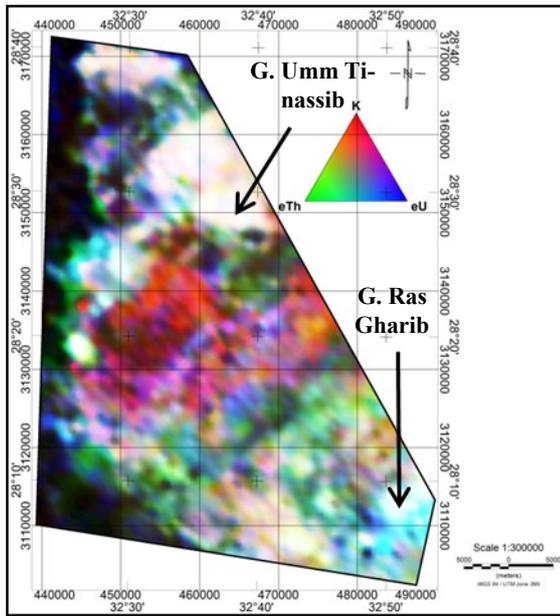
128

Figure 8. False color radioelements ternary image of West Ras Gharib area, North Eastern Desert, Egypt.

with different radioactive decay processes all are absorbed in rocks and finally transformed into heat that can be generally calculated from the following equation (L Rybach, 1988):

$$A(\mu Wm\text{-}3)=\rho(0.0952CU+0.0256CTh+0.0348CK\ldots\ldots\ldots\ldots(1)$$

Where; ρ is the density of rock (in kilograms per cubic meter), CU and CTh are the concentrations of uranium and thorium (in parts per million), CK is the concentration of potassium (in weight percent), the constants 0.0952, 0.0256 and 0.0348 are the radiogenic heat generation rate per mass of uranium, thorium and potassium respectively (L Rybach, 1988).

According to previous equation the density and the concentration of radioelements U, Th and K in the rock is required. The concentrations of radioelements measured in the laboratory has been used to calculate RHPR (Fernàndez et al., 1998) and directly from gamma ray logs (Bücker and Rybach, 1996). Salem et al (2004) averaged roughly the density for each rock unit from the densities of rocks given by (Shaaban, 1973) (Table 6).

The radioactive heat production varies greatly with rock type and the results shows good correlation between the radioactive heat production map (Fig. 9) and the geological map in (Fig.3). The area possesses a range of radioactive heat production varying from 0.17μWm-3 to 4.80μWm-3. The higher average values are obtained for younger granitic rocks (at G. Umm Tinassib and west G. Ras Gharib) (1.60 - 4.80 μWm-3), whereas the lowest average value is obtained for sedimentary rocks at the western part of the study area and ranging from (o.17 to 0.96 μWm-3) and the intermediate average values are obtained for (older granitic rocks, Dokhan volcanics and metavolcanics) and ranging from (0.99 – 1.55 μWm-3) The variation and irregularity in the distribution of the natural radioelements radioactive heat production due to the dissimilarity in the geochemical behavior of U, Th, and K.

The RHP anomalous zones A and B (whose RHP values high and up to 4.80 μWm3) located at G. Umm Tinassib (and

Table 6. Average density for each rock unit (Shaaban, 1973)

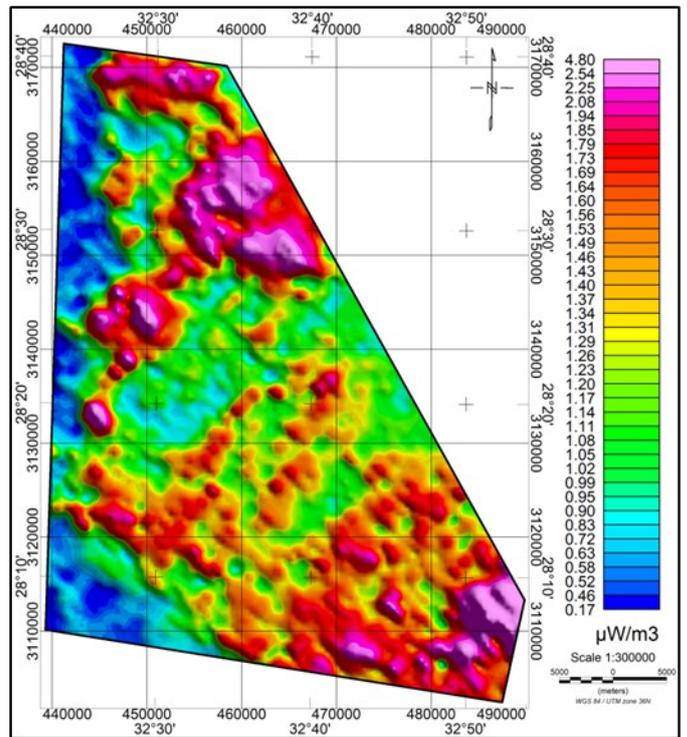| Rock Units	Density (g/cm^3)
Sedimentary	2.41
Metavolcanic	2.64
Dokhan volcanic	2.6
Granite	2.59
Gabbro &Metagabbro to metadiorite	2.88

Figure 9. Filled color map of radioactive heat production of West Ras Gharib area, North Eastern Desert, Egypt.

its SW extension) and W. G. Ras Gharib area (Fig. 9). On the other hand, RHP values are altered less than the threshold value especially within older granite and sedimentary rock units. This is clearly related to their less content of radionuclides, eU, eTh and K.

Calculating Land Surface Temperature (LST) from ASTER-TIR and Landsat 8-TIR Data

The radiation emitted from a surface in the TIR wavelengths is a function of both the surface temperature and emissivity. The emissivity relates to the surface composition and is frequently used for mapping surface constituent. There are some techniques to separate the emissivity and temperature information in radiance data measured with TIR sensors, e.g. reference channel emissivity and emissivity normalization techniques, which assume a fixed emissivity value and pro-duce emissivity and temperature outputs (Hook et al., 1992; Kealy and Hook, 1993) . In current study the Reference Channel Emissivity technique was applied to calculate emissivity and temperature values from thermal infrared radiance data. The Reference Channel Emissivity method supposes that all the pixels in one channel (band) of the thermal infrared data have a constant emissivity. Using this constant emissivity, a

temperature image is calculated, and those temperatures are used to calculate the emissivity values in all other bands using the Planck function (EXELISVIS ENVI, 2012).

In case of ASTER-TIR band 10 has been selected (whose center wavelength of 8.2910 μm) as a reference channel and in case of Landsat 8-TIR, band 10 (whose center wavelength of 10.80 μm) has been selected as a reference channel. And enter the desired emissivity value (0.96) chosen in case of ASTER-TIR data as it is the average emissivity value of distilled water of Johns Hopkins University (JHU) spectral library at the selected wavelength. The same method was applied on the Landsat 8-TIR data. (Figures.10 A&B) shows the calculated ASTER-TIR and Landsat-8-TIR Land Surface Temperature as grey scale color, respectively. ASTER-TIR Land Surface Temperature (AST-LST)

ranges between 27.64oC to 47.2oC (Fig.10 A). On the other hand, the Landsat 8-TIR Land Surface Temperature (LS8-LST) ranges between 30.64oC to 50.68oC (Fig.10 B). (Figures-11 A & B) represents the calculated ASTER-TIR and Landsat-8-TIR Land Surface Temperature as thermal scale color, respectively. The positive relation between ASTER-TIR-LST and Landsat 8-TIR-LST are showed in (Fig. 12).

Relation Between Radiogenic Heat Production and Land Surface Heat Temperature

When comparing the RHP (Fig. 9) with the calculated satellite land surface heat temperature (both ASTER and Landsat 8 TIR data) we found there were no specific relationship or very weak parallel relationship (when the value of the Y-axis is constant, there are multiple values on X
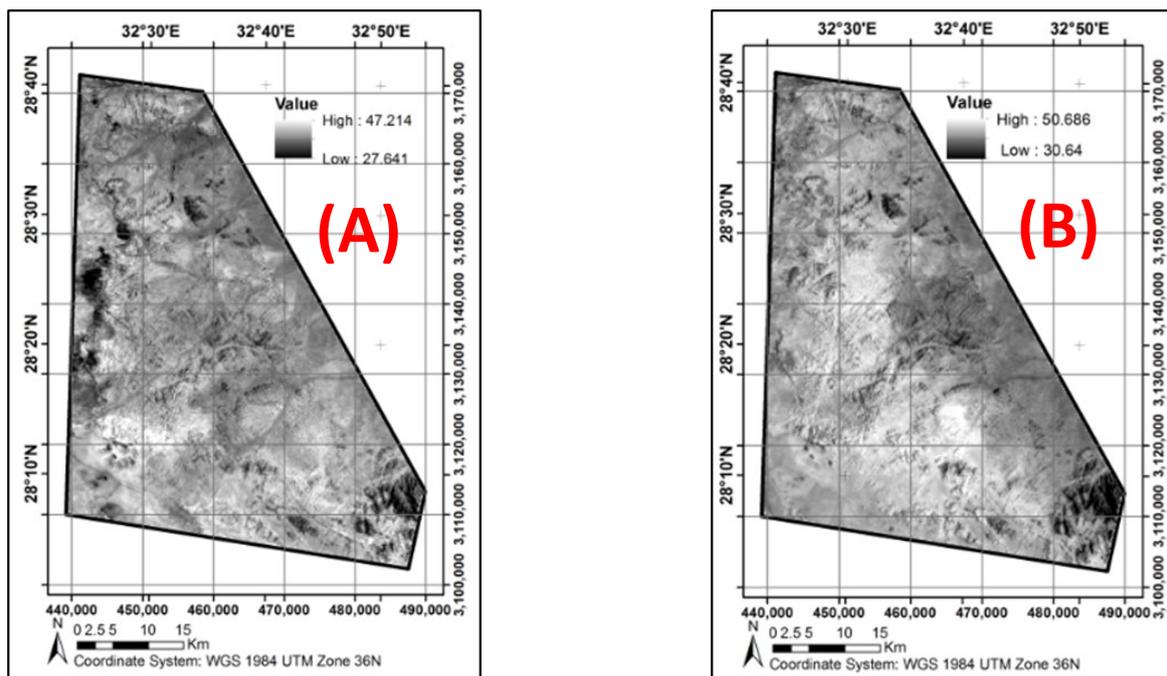

Figure 10. Resulted land surface temperature in Celsius for both (A) ASTER-TIR and (B) Landsat 8-TIR data respectively as grey scale color of west Ras Gharib area, North Eastern Desert, Egypt.
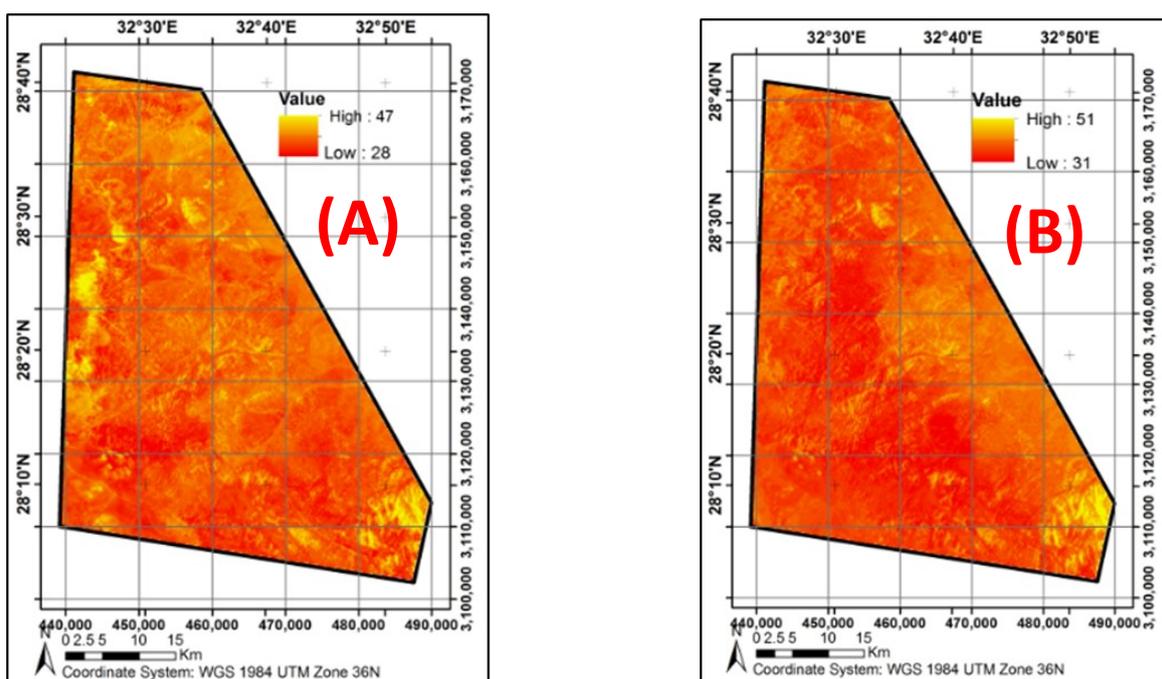

Figure 11. Resulted land surface temperature in Celsius for both (A) ASTER-TIR and (B) Landsat 8-IR data respectively as thermal scale color of West Ras Gharib area, North Eastern Desert, Egypt.

Table 7. Resulted Radiogenic Heat Production Rate and Land Surface Heat Temperature (ASTER & Landsat-8) for TheRock Units of The Study Area:

Rock Units	Statistical Parameters	RHPR	Landsat-8_LST	ASTER_LST
Quaternary Wadi deposits (Qw)	Min	0.281	38.327	27.987
	Max	3.404	50.686	44.127
	Mean	1.310	44.907	39.159
	STDEV	0.471	1.942	1.701
Quaternary (Q)	Min	0.38	38.492	28.402
	Max	2.867	48.261	44.229
	Mean	1.130	44.676	39.503
	STDEV	0.399	1.478	1.521
Thebeth Group (Tetz)	Min	0.506	40.035	33.974
	Max	1.79	46.108	40.414
	Mean	1.235	43.161	37.505
	STDEV	0.347	1.178	1.063
Sudr Formation "Kus"	Min	0.402	38.554	33.672
	Max	0.769	44.791	39.135
	Mean	0.571	41.867	36.741
	STDEV	0.086	1.342	1.210
Galala Formation "Kug"	Min	0.234	39.3	31.855
	Max	1.81	47.822	43.841
	Mean	0.545	44.277	40.114
	STDEV	0.139	1.153	1.490
Galala, Umm Omeiyed and Rakhiyat Fm (Kuyb)	Min	0.328	39.683	35.952
	Max	0.824	47.019	41.529
	Mean	0.518	43.637	38.483
	STDEV	0.091	1.212	0.980
Wadi Qena Formation (Klq)	Min	0.299	39.15	29.3
	Max	2.254	47.656	43.094
	Mean	0.669	43.753	37.056
	STDEV	0.241	1.50	2.530
Samr el-Qaa Formation (Cq)	Min	0.322	39.198	27.758
	Max	2.098	48.329	44.43
	Mean	0.916	44.376	36.220
	STDEV	0.331	1.458	2.682
Araba Formation (Es)	Min	0.507	38.336	30.764
	Max	3.725	48.681	47.214
	Mean	1.144	45.107	38.611
	STDEV	0.399	1.678	2.560
Dokhan Volcanics (Vd)	Min	0.712	38.924	29.5
	Max	2.227	49.187	47.035
	Mean	1.505	44.978	40.276
	STDEV	0.305	1.751	2.354
Younger Granite (gβ)	Min	0.72	30.64	27.641
	Max	5.381	49.657	44.653
	Mean	2.003	43.478	38.375
	STDEV	0.613	2.694	2.279
Weathered Older Granite (gαw)	Min	0.714	41.244	32.989
	Max	1.896	48.313	44.475
	Mean	1.249	44.991	37.499
	STDEV	0.204	1.068	1.860
Older Granite (gα)	Min	0.481	35.361	32.063
	Max	4.803	50.429	45.459
	Mean	1.364	45.226	39.651
	STDEV	0.351	2.080	1.537

-axis) between these two components, in other words hotter regions are not restricted to those of higher RHP rates and vice versa. This may be due to the considerable low RHP magnitude (≤ 4.8 µW/m3), which is not sufficient to be translated into a remotely sensed surface temperature. (Figures 13 and 14) represent the relationship between ASTER-TIR-LST with RHP & the relationship between Landsat 8-TIR-LST with RHP respectively. Table 7 shows the result values of both radiogenic heat production and land surface heat temperature (ASTER and Landsat-8) for each rock units covering the study area.

Factors Affecting Surface Heat Temperature

Some factors affect Earth's surface temperatures by influencing the amount of solar radiation that strikes the surface or by trapping the earth's radiation. One or more factor of the following will do:

Figure 12.The relation between the calculated LST of ASTER-TIR and Landsat 8-TIR data of West Ras Gharib area, North-eastern Desert, Egypt.

Figure 13. The relation between the calculated LST of ASTER-TIR data and radiogenic heat production of West Ras Gharib area, North Eastern Desert, Egypt.

Figure 14. The relation between the calculated LST of Landsat 8-TIR data and radiogenic heat production of West Ras Gharib area, North Eastern Desert, Egypt.

Topography

Differences in topography cause local variations in the incident angle at which the sun's radiation strikes the ground surface; the lower the angle the less solar radiation per unit area and the lower surface temperature.

Shading and Scattering

In mountainous regions, higher ridges shield lower elevation surfaces from incoming radiation, and reduce the hours of sunshine. In addition, different atmospheric scattering types due to clouds, smoke or dust reduce the solar radiation reach the earth's surface and accordingly reduce the surface temperature.

Moisture

The more moisture rock contains the greater its ability to absorb energy and become a good emitter. Wet rocks have a high emissivity similar to water (Jensen, 2007).

Rock Density

It is a function in thermal heat capacity (the ability of the rock to store heat) and thermal inertia (the ability of the rock to resist change in its temperature). Denser rock will have greater thermal inertia; hence will still be warmer for longer time and vice versa.

Rock Color Tone

Darker colored objects are usually better absorbers and emitters (i.e. they have a greater emissivity) than brighter colored objects which tend to reflect more of the incident energy.

Wind Effect

Strong daytime winds near the surface tend to prevent high surface temperatures. Transfer of heat between the surface and the air is improved by mixing, which carries heat away from the heated surfaces. This air movement also transports moisture, increasing evaporation from moist surfaces and thus restricting the temperature rise. At night, the effect of strong winds is to prevent low surface temperatures by mixing warmer air downward and bringing it into contact with the surface, where some of the heat can be transferred to the ground by conduction. Thus, windiness has a moderating influence on surface temperatures (Shroeder and Buck, 1970).

Conclusions

The present study investigated the relationship between the RHPR, which are derived from Rybach equation using air-borne measured equivalents of radionuclides (eU, eTh and K) and the measured rock densities, with the calculated land surface heat temperature, that are derived from the satellite thermal bands of (ASTER-TIR) and (Landsat-8-TIR). After calculations, two zones (A&B) which associated with younger granite were found to have the highest radioactivity and accordingly the highest RHPR. The RHPR threshold value reached 4.8µW/m3; this can limitedly influence surface temperatures with levels difficult to be recognized on satellite remote sensing scale.

Using thermal bands of both (ASTER-TIR) and (Landsat-8-TIR), surface emissivity and land surface heat temperatures of the study area were calculated. For the overall rock
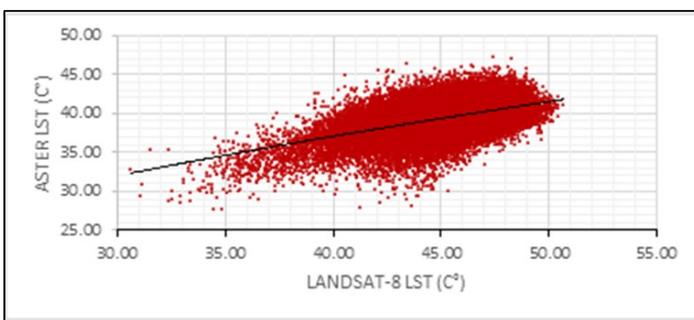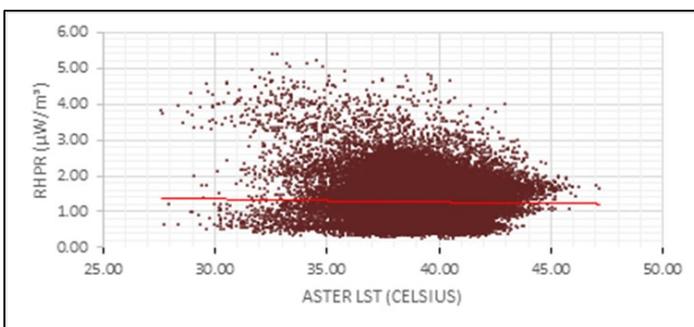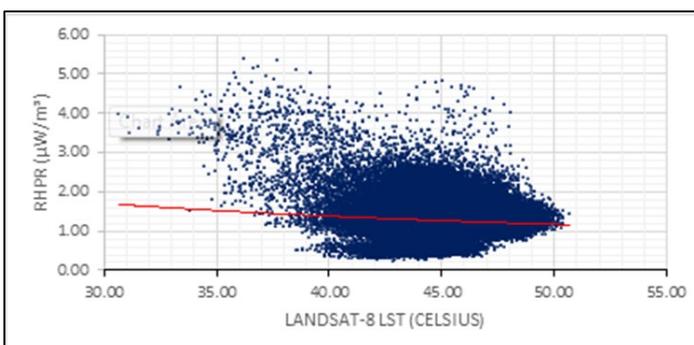
coverage in the area, ASTER-TIR Land Surface Temperature (AST-LST) ranges between 27.64oC to 47.2oC. On the other hand, the Landsat 8-TIR Land Surface Temperature (LS8-LST) ranges between 30.64oC to 50.68oC, showing weak or to some extent parallel correlation with RHP values. There are a number of factors that may affect the land surface heat temperature by several magnitudes than RHPR, e.g. topography, shading and scattering, moisture, rock density, rock color tone and wind effect. All these factors should be taken into consideration, when studying thermal properties of rocks and compare it with the radioactive properties.

So, there is a theoretical relationship that is difficult to measure from the thermal data of ASTER and Landsat-8. This is because the heat flux resulting from the radiation is very weak and can't be monitored virtually from satellite images due to the presence of other factors more affecting the temperature of the surface of the rock. The most important of these factors is basically the scarcity of high radioactive concentrations in the study area.

Acknowledgment

Reference

Adagunodo, T. ., Bayowa, O. G., Usikalu, M. R., & Ojoawo, A. I. (2019). Radiogenic Heat Production in The Coastal Plain Sands of Ipokia, Dahomey Basin, Nigeria. MethodsX, 6, 1608–1616. https://doi.org/10.1016/j.mex.2019.07.006

Ammar, A., Abdelrahman, E., Hassanein, H. and Soliman, K. (2007) Separation of aerial radiospectrometric zones using least-square method on a sample area in Egypt. King Abdul-Aziz University, Faculty of Earth Science. The Arabian Journal for Science and Engineering. Volume 32, number 1A.

BEA, F. (1996). Residence of REE, Y, Th and U in Granites and Crustal Protoliths; Implications for the Chemistry of Crustal Melts. Journal of Petrology, 37(3), 521–552. https://doi.org/10.1093/petrology/37.3.521

Bücker, C., & Rybach, L. (1996). A Simple Method to Determine Heat Production from Gamma-Ray Logs. Marine and Petroleum Geology, 13(4), 373–375. https://doi.org/10.1016/0264-8172(95)00089-5

Bühler, B., Breitkreuz, C., Pfänder, J. A., Hofmann, M., Becker, S., Linnemann, U., & Eliwa, H. A. (2014). New Insights into The Accretion of The Arabian-Nubian Shield: Depositional setting, composition and geochronology of a Mid-Cryogenian arc succession (North Eastern Desert, Egypt). Precambrian Research, 243, 149–167. https://doi.org/10.1016/j.precamres.2013.12.012

Cermak, V., Huckenholz, H., Rybach, L., & Schmid, R. (1982). Radioactive Heat Generation in Rocks. In: Hellwege, K. (eds), Landolt–Börnstein Numerical Data and Functional Relationships in Science and Technology. Geophysics and Space Research, 1(Supvolume b; Chapter 4.4), 433–481.

Clauser, C. (2011). Radiogenic Heat Production of Rocks. In Encyclopedia of Solid Earth Geophysics . In: Gupta H (ed) (2nd ed.). Springer, Dordrecht.

Conoco, C. (1987). The Egyptian General Petroleum Corporation. Geological Map of Egypt, Scale 1: 500,000.

Coolbaugh, M., Kratt, C., Fallacaro, A., Calvin, W., & Taranik, J.

(2007). Detection of Geothermal Anomalies Using Advanced Spaceborne Thermal Emission and Reflection Radiometer (ASTER) Thermal Infrared Images at Bradys Hot Springs, Nevada, USA. Remote Sens Environ, 106(3), 350–359.

Drury, S. A., & Walker, A. S. D. (1987). Display and En

hancement of Gridded Aeromagnetic Data of the Solway Basin. International Journal of Remote Sensing, 8(10), 1433–1444. https://doi.org/10.1080/01431168708954787

El-Said. (2014). The Application of Thermal Remote Sensing Imagery for Studying Uranium Mineralization: A New Exploratory Approach for Developing the Radioactive Potentiality at El-Missikat and El-Eridiya District, Central Eastern Desert, Egypt. Damietta University.

Eneva, M., & Coolbaugh, M. (2009). Importance of Elevation and Temperature Inversions for The Interpretation of Thermal Infrared Satelite Images Used in Geothermal Exploration. GRC Transactions, 33, 467–470.

Eneva, M., Coolbaugh, M., Bjornstad, S., & Combs, J. (2007). Detection of Surface Temperature Anomalies in The Coso Geothermal Field Using Thermal Infrared Remote Sensing. GRC Transaction, 31.

Erdi-Krausz, G., Mantolin, M., Minty, B., Nicolet, J., Reford, W. ., & Schetselaar, E. (2003). Guidelines for Radioelement Mapping Using Gamma Ray Spectrometry Data : Also as Open Access E-Book. International Atomic Energy Agency (IAEA).

Farag, T., Soliman, N., El Shayat, A., & Mizunaga, H. (2020). Comparison Among The Natural Radioactivity Levels, The Radiogenic Heat Production, and The Land Surface Temperature in Arid Environments: A Case Study of The El Gilf El Kiber Area, Egypt. Journal of African Earth Sciences, 172, 103959. https://doi.org/10.1016/j.jafrearsci.2020.103959

Farr, T. G., & Kobrick, M. (2000). Shuttle Radar Topography Mission Produces a Wealth of Data. Eos, Transactions American Geophysical Union, 81(48), 583. https://doi.org/10.1029/EO081i048p00583

Farr, T. G., Rosen, P. A., Caro, E., Crippen, R., Duren, R., Hensley, S., Kobrick, M., Paller, M., Rodriguez, E., Roth, L., Seal, D., Shaffer, S., Shimada, J., Umland, J., Werner, M., Oskin, M., Burbank, D., & Alsdorf, D. (2007). The Shuttle Radar Topography Mission. Reviews of Geophysics, 45(2), RG2004. https://doi.org/10.1029/2005RG000183

Fernàndez, M., Marzán, I., Correia, A., & Ramalho, E. (1998). Heat Flow, Heat Production, and Lithospheric Thermal Regime in The Iberian Peninsula. Tectonophysics, 291(1–4), 29–53. https://doi.org/10.1016/S0040-1951(98)00029-8

Gupta, H., & Roy, S. (2007). Geothermal Energy: An Alternative Resource for The 21st Century. Elsevier B.V.

Hook, S. J., Gabell, A. ., Green, A. ., & Kealy, P. . (1992). A Comparison of Techniques for Extracting Emissivity Information from Thermal Infrared Data for Geologic Studies. Remote Sensing of Environment, 42(2), 123–135. https://doi.org/10.1016/0034-4257(92)90096-3

Jaupart, C., Labrosse, S., Lucazeau, F., & Mareschal, J.-C. (2015). Temperatures, Heat, and Energy in the Mantle of the Earth. In Treatise on Geophysics (pp. 223–270). Elsevier. https://doi.org/10.1016/B978-0-444-53802-4.00126-3

Jensen, J. (2007). Remote Sensing of The Environment: An Earth Resource Perspective. Prentice-Hall, Upper Saddle River.

Kealy, P. S., & Hook, S. J. (1993). Separating Temperature and Emissivity in Thermal Infrared Multispectral Scanner Data: Implications for Recovering Land Surface Temperatures. IEEE Transactions on Geoscience and Remote Sensing, 31(6), 1155–1164. https://doi.org/10.1109/36.317447

Kobrick, M. (2006, March). On The Toes of Giants-How SRTM was Born. Photogrammetric Engineering and Remote Sensing.

Mather, P. M., & Koch, M. (2011). Computer Processing of Remotely-Sensed Images: An Introduction (4 (ed.)). Wiley-Blackwell.

McDonough, W. F., & Sun, S. -s. (1995). The Composition of The

Earth. Chemical Geology, 120(3–4), 223–253. https://doi.org/10.1016/0009-2541(94)00140-4

Pasquale, V., Verdoya, M., & Chiozzi, P. (1999). Thermal State and Deep Earthquakes in the Southern Tyrrhenian. Tectonophysics, 306(3–4), 435–448. https://doi.org/10.1016/S0040-1951(99)00070-0

Pasquale, V., Verdoya, M., & Chiozzi, P. (2001). Heat Flux and Seismicity in The Fennoscandian Shield. Physics of the Earth and Planetary Interiors, 126(3–4), 147–162. https://doi.org/10.1016/S0031-9201(01)00252-7

Pleitavino, M., Carro Pérez, M. E., García Aráoz, E., & Cioccale, M. A. (2021). Radiogenic Heat Production in Granitoids from The Sierras de Córdoba, Argentina. Geothermal Energy, 9(1), 16. https://doi.org/10.1186/s40517-021-00198-9

Pour, A. B., & Hashim, M. (2012). The Application of ASTER Remote Sensing Data to Porphyry Copper and Epithermal Gold Deposits. Ore Geology Reviews, 44, 1–9. https://doi.org/10.1016/j.oregeorev.2011.09.009

Prakash, A. (2000). Thermal Remote Sensing: Concepts, Issues and Applications. International Archives of Photogrammetry and Remote Sensing, 33(B1), 239–243.

Rosen, P., & et al. (2000). Synthetic Aperture Radar Interferometry. In Proceedings of The IEEE, 88(3), 333–382.

Rybach, L. (1988). Determination of Heat Production Rate. Kluwer, Dordrecht.

Rybach, Ladislaus. (1976). Radioactive Heat Production in Rocks and Its Relation to Other Petrophysical Parameters. Pure and Applied Geophysics PAGEOPH, 114(2), 309–317. https://doi.org/10.1007/BF00878955

Said, R. (1990). The Geology of Egypt. A.A. Balkema.

Salem, A., Elsirafy, A., Aref, A., Ismail, A., Ehara, S., & Ushijima, K. (2004). Estimation of Radioactive Heat Production from Airborne Spectral Gamma-Ray Data of Gebel Duwi Area, Egypt. Memoirs of the Faculty of Engineering, Kyushu University, 64(2), 135–146.

Shaaban, M. (1973). Geophysical Studies on The Lead Zinc Mining District between Quseir and Mersa Alam, Red Sea Coast, Eastern Desert, Egypt. Cairo University.

Stacey, F., & Davis, P. (2008). Physics of The Earth. Cambridge University Press.

Van-Schmus, W. (1984). Radioactivity Properties of Minerals and Rocks. CRC Press.

Wulder, M. A., Loveland, T. R., Roy, D. P., Crawford, C. J., Masek, J. G., Woodcock, C. E., Allen, R. G., Anderson, M. C., Belward, A. S., Cohen, W. B., Dwyer, J., Erb, A., Gao, F., Griffiths, P., Helder, D., Hermosilla, T., Hipple, J. D., Hostert, P., Hughes, M. J., … Zhu, Z. (2019). Current Status of Landsat Program, Science and Applications. Remote Sensing of Environment, 225, 127–147. https://doi.org/10.1016/j.rse.2019.02.015

Zhang, B. T., Wu, J., Ling, H., & Chen, P. (2007). Estimate of Influence of U-Th-K Radiogenic Heat on Cooling Process of Granitic Melt and Its Geological Implications. Sci China Ser D-Earth Sci, 5(5), 672–677.